JOURNAL OF AIRCRAFT
Vol. 47, No. 1, January–February 2010

Videogrammetry Dynamics Measurements of a Lightweight Flexible Wing in a Wind Tunnel

Jonathan T. Black,* Nathan A. Pitcher,† Mark F. Reeder,‡ and Raymond C. Maple§
Air Force Institute of Technology, Wright–Patterson Air Force Base, Ohio, 45433

DOI: 10.2514/1.44545

Videogrammetry is a measurement technique well suited to characterizing lightweight, flexible wings in wind-tunnel testing. It is noncontact, full field, and can capture the large-amplitude deflections experienced by the wings. Here videogrammetry is used to analyze the spectral content of the motion of a flexible Nighthawk mini-unmanned aerial vehicle wing and animate the operating deflection shapes of the wing corresponding to structural resonance frequencies. The wing was tested at angles of attack ranging from −5 to 13 deg and wind speeds ranging from 20 to 40 mph. Results show that the flexible wing tends to experience flapping behavior at frequencies much lower than structural resonance at low angles of attack. This behavior is confirmed by the spectral content of the wing displacements and the corresponding animated deflection shapes. This analysis uses videogrammetry data in the spectral analysis and visualization of resonance shapes. The data are necessary to validate numerical models of the wings, understand complicated membrane-structure interactions, and optimize wing performance in different flight regimes.

I. Introduction

UNMANNED aerial vehicles (UAVs) are aircraft with a host of potential military and civilian applications. The size of current UAVs varies widely, with wingspans ranging from approximately 18 cm to 40 m. Mini-UAVs, defined here as having wingspans ranging from 0.5 to 3.5 m, currently in the field are predominately used for surveillance and reconnaissance. The Nighthawk mini-UAV shown in Fig. 1 was designed for aerial surveillance. It has a removable 66-cm-span wing that can be stored in-line with the aircraft, carries forward- and side-facing cameras and a side-facing thermal imager, weighs 0.68 kg (1.5 lb), and flies at wind speeds of 18–40 kt (30–75 km/h). It exploits Global Positioning System and autopilot technology for navigation, has a loiter time of 70–90 min, and a range of 2–10 km.

Videogrammetry is the science of making time history measurements from synchronized videos from multiple cameras imaging the same object. Wing deformation during wind-tunnel testing has been measured for several years at NASA Langley Research Center, initially with a single camera at 15 frames per second (fps) and coarse target grids and progressing to faster synchronized multicamera systems [1,2]. The twist of deformable wings has been measured in wind tunnels using videogrammetry and its static counterpart photogrammetry [3]. Videogrammetry has also been used to measure resonance frequencies of aeroelastic models [4]. Three-dimensional surface measurements of static-deflected shape and strain in wind tunnels have been taken using multicamera video speckle tracking, also called visual image correlation, videogrammetry, and projection moiré interferometry [5–8]. These studies found significant billowing, bending, and washout occurring in lightweight and flexible wings, making these kinds of image-based measurements valuable tools.

These techniques exhibit a range of applications and measurement resolutions. Wind-tunnel measurements of rigid models on the order of several meters, in which deflection measurements on the order of millimeters are desired, require stringent and precise calibration that can be time consuming [1,2]. As videogrammetry is used more frequently to measure lightweight aerospace structures that experience greater deflections, consumer software has become capable of providing faster and easier solutions with sufficient accuracies on the order of 1/1000 of the test article size or better [9–11].

Current development of small UAVs with very flexible composite wings and even flapping-wing micro-UAVs (MAVs) requires measurement techniques analogous to those that biologists use to analyze the flight mechanics of animals. For example, researchers at Brown University have used multiple video cameras framing at up to 500 fps to measure the wing and body angles of bats in flight [12,13]. Similar measurements have been used to study the flight characteristics of moths and birds [14–16]. Investigations of flapping-wing MAVs have involved the stereo tracking of speckle patterns on the wings to produce deformation and in-plane strain measurements [5] and the projection of targets onto the wings [17].

Videogrammetry has also been used to measure both the resonance frequencies and corresponding operating deflection shapes (ODSs) of large, lightweight, flexible membrane-based space structures. Again, this measurement technology is well suited to such challenging structures because it is noncontact and, therefore, does not change the mass or stiffness of the object being measured and captures low-frequency large-amplitude motion [9–11]. As mini-UAV and MAV development trends toward lighter, membrane-based, and even flapping wings, such experimental techniques can provide valuable data.

The purpose of this study is to use noncontact videogrammetry measurement techniques to characterize the dynamic behavior of flexible, lightweight mini-UAV wings undergoing wind-tunnel tests. It will use noncontact videogrammetry measurement to analyze the resonance frequencies and corresponding ODS of the Nighthawk wings. Knowledge of the deflection shape of the wing at different resonance frequencies is necessary to validate structural, aeroelastic, and aerodynamic numerical models; optimize wing aerodynamic performance as a function of angle of attack (AOA), Reynolds number (Re), and geometry; and control flutter. Previous efforts to

Presented as Paper 2416 at the 50th AIAA/ASME/ASCE/AHS/ASC Structures, Structural Dynamics, and Materials Conference 17th AIAA/ASME/AHS Adaptive Structures Conference 11th AIAA No, Palm Springs, CA, 4–7 May 2009; received 23 March 2009; revision received 17 June 2009; accepted for publication 18 June 2009.

*Assistant Professor, Department of Aeronautics and Astronautics, 2950 Hobson Way. Member AIAA.
†Research Engineer, Computational Sciences Branch, U.S. Air Force Research Laboratory/Air Vehicles Directorate, 2210 8th Street, Building 146. Member AIAA.
‡Associate Professor, Department of Aeronautics and Astronautics, 2950 Hobson Way. Member AIAA.
§Assistant Professor; currently Research Engineer, Hawker Beechcraft, Inc., Wichita, Kansas 67201. Senior Member AIAA.

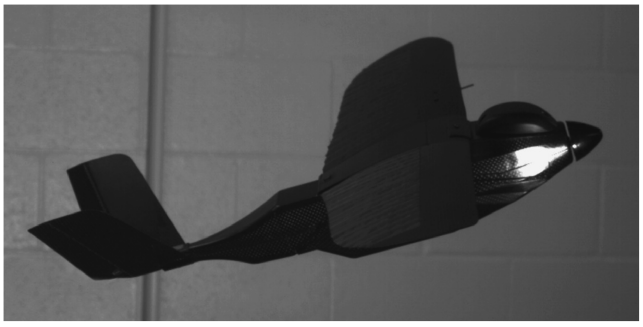

Fig. 1 Nighthawk mini-UAV.

characterize the performance of the Nighthawk mini-UAV measured the static wing deflection at various AOA to analyze the lift, drag, and pressure distributions through computational fluid dynamics (CFD) [18–20].

II. Test Setup

A production model Nighthawk was provided by Applied Research Associates for wind-tunnel testing. The model has no internal components other than the motor for the propeller on which the nose spinner is mounted. It is 51 cm long with a 66 cm wingspan. The Nighthawk's body is composed of a carbon fiber composite. The leading edge of the lightweight and flexible wing and the wing ribs are also made of carbon fiber, whereas the gaps between the ribs are spanned by nylon cloth. The root chord is 15.25 cm, the planform area of the wing is 0.0457 m^2, and the aspect ratio is 4.8. The root camber of the undeflected wing is approximately 7.8%. The incidence angle is approximately 4.8 deg, and the dihedral of the undeflected wing is approximately 4.9 deg. Typical Reynolds numbers range from 90,000 to 180,000.

Flexible wings offer several advantages over rigid wings. Smoother flight and greater stall resistance at high AOA are both products of adaptive washout. Adaptive washout occurs when a flexible wing deforms due to the aerodynamic loads experienced during flight. At high AOA or increased airspeed, the wing will decamber and twist forward, reducing the apparent AOA at the wing tip, providing increased stall resistance and improved gust response. Another advantage of a flexible wing is increased roll stability. The wing tips of a flexible-wing aircraft will deflect upward during flight due to the lift on the wings, increasing dihedral and resulting in greater roll stability [21,22]. Studies on rigid and flexible versions of wings of the same geometry as tested here confirm that the flexible wings showed increased stability in roll, pitch, and yaw, improved efficiency in the form of a higher lift to drag ratio, and improved portability, and found that washout in the flexible wing can delay the onset of stall [23].

Three significant changes were made to the Nighthawk before testing began. The mini-UAV was fitted with an internal mounting block, the upper wing surface was marked with high-contrast targets for videogrammetry measurement, and the propeller blades were removed to compare more closely with the CFD model [18]. The ruddervators were free throughout all tests.

Two types of high-contrast targets were attached the upper wing surface: noncoded targets (dots) and coded targets (dots surrounded by banded sections). The noncoded targets are bright yellow circles 0.635 cm in diameter. This size was selected to ensure the diameters were at least 8–10 pixels in photographs, which is ideal for automatic target recognition during image processing [24]. The coded targets are automatically recognized by the processing software and are used to orient the photos (cameras).

All attached targets were low profile to minimize their impact on airflow over the wing. Targets were only attached to the carbon fiber composite leading edge and ribs to avoid altering the mass and stiffness of the nylon cloth and ensure that the structural motion of the wing was captured. Figure 2 shows the close spacing of the wing ribs, indicating that the wing's behavior will be dominated by them. The targets were positioned on the wing in rows spaced approximately 2.5 cm apart, with the first row starting 1.25 cm behind the leading edge. This spacing ensured easy sorting of the targets during post-processing. Figure 2 shows the Nighthawk after it was marked with targets.

Testing was conducted in the low-speed open-circuit wind tunnel shown in Fig. 3. The test section is 1.12 m wide, 0.79 m high, and 1.83 m long. Maximum airspeed in the test section is 240 km/h. There are four antiturbulence screens and an aluminum honeycomb flow straightener, and the measured freestream turbulence is 2.25%. There are windows on the ceiling and on each side of the test section, and it has a white floor, which contrasts well with the black wing of the Nighthawk. However, at moderate speeds and AOA, washout occurred and the targets near the leading edge of the wing blended into the wind-tunnel floor when viewed from above. To provide contrast for the targets on the leading edge, black felt was attached to the floor of the wind tunnel, ensuring target recognition despite washout.

Six coded targets were secured to the wind-tunnel floor to act as reference points during postprocessing (labeled 1–6 in Fig. 4). These targets were visible in each camera. Targets 1 and 2 define the x axis (positive from 2 to 1) and the scaling factor because they are separated by 47.1 cm. Targets 2 and 3 define the y axis (positive from 2 to 3). The z axis is normal to the wind-tunnel floor (up is positive).

At AOA less than 4 deg, the targets on the wing lie in a plane approximately 38 cm above the wind-tunnel floor. The only targets out of this plane were the coded targets used to define the scale and axes. Because of the three-dimensional nature of the videogrammetry process, difficulty can occur when measuring planar

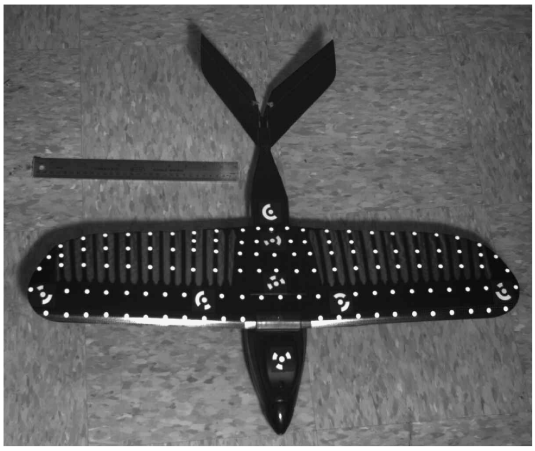

Fig. 2 Nighthawk mini-UAV wing marked for videogrammetry.

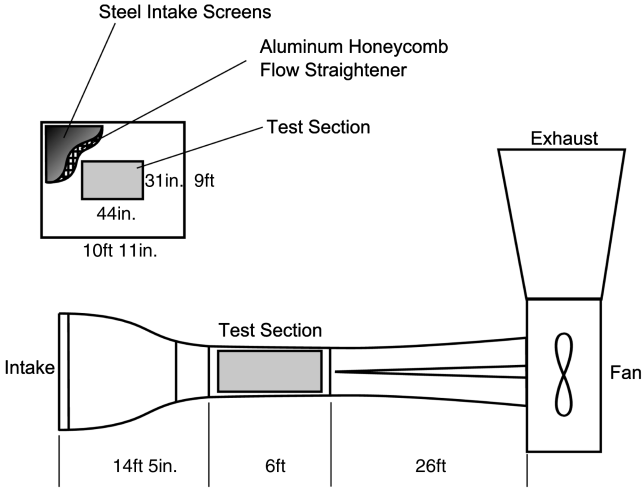

Fig. 3 Wind tunnel schematic [23].

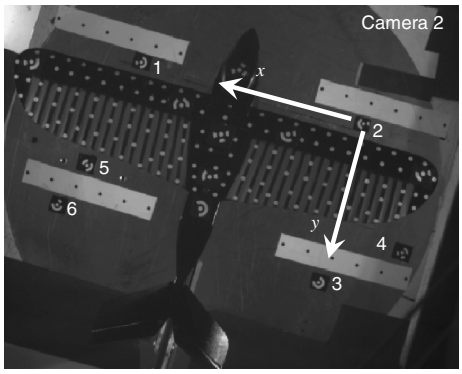

Fig. 4 Image from videogrammetry camera 2 used in processing.

objects due to a lack of information about the out-of-plane dimension. Noncoded targets were therefore added to the wind-tunnel floor (Fig. 4) to maintain accuracy and aid in solution convergence by providing out-of-plane measurement points.

Three synchronized Basler 501k high-speed digital cameras captured image sequences during wind-tunnel testing. Each camera is capable of capturing a maximum 75 fps at maximum resolution of 1280×1024 pixels. A custom computer workstation was used to drive the cameras and store image sequences. Each camera was connected to its respective video capture board in the PC. Image capture software controlled the cameras via their respective video capture boards.

For optimal viewing of the wing, all cameras were positioned atop the wind tunnel and aimed through the viewing glass above the test section (Fig. 5). They were positioned in-line with the flow direction with camera 1 in front of the Nighthawk, camera 2 directly above the Nighthawk, and camera 3 trailing the Nighthawk. There was at least a 30 deg separation angle between the cameras. The cameras were positioned far enough from the model to allow each camera a full view of the wing. Figure 5 illustrates the viewing angle of each camera.

To provide accurate three-dimensional data in time, it was important to ensure the cameras were synchronized. The first camera was configured as the master and the other two were slaves. A synchronization test was performed in which the captured image size was reduced to 480×480 pixels to increase the frame rate to 156 fps. The collected image sequences were examined to verify that any discrepancy between the cameras was substantially less than the frame rate. Note the wind-tunnel tests performed here were recorded at 75 fps.

Each of the three cameras was calibrated to remove image distortions caused by camera aberrations. This process calculates the focal length (zoom), location of the principal point, radial lens distortion, and decentering lens distortion of each camera, enabling accurate photographic measurements by compensating for any deviation of the recorded image from what would have been recorded by an ideal pin-hole camera.

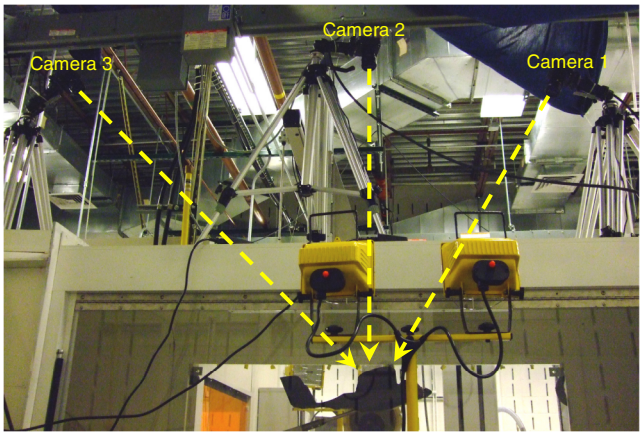

Fig. 5 Videogrammetry camera setup above wind tunnel imaging Nighthawk mini-UAV.

Following calibration, a test was performed to ensure the wind-tunnel glass did not distort the images and decrease measurement accuracy. This test involved capturing image sets of a precisely machined calibration slate. The calibration slate is black with small white targets in a grid measuring 135×80 mm. It is not typically used for camera calibration; however, because it has precisely located targets, it was useful in a test to determine the accuracy of the videogrammetry measurements. It was placed in the wind tunnel at about the same height as the wing. Image sets of the calibration slate were captured. The coded targets on the floor were used to scale the images, and the size of the calibration grid was measured using videogrammetry. Because the calibration slate is smaller than the wing, the test was performed several times with the calibration sheet moved to different positions covering the same field of view occupied by the wing. The maximum error measured in these tests was 0.62 mm. This error is acceptable because tip deflection is expected to be as high as 5 cm.

Proper lighting is paramount in capturing high-quality images. The lighting was required to illuminate the high-contrast targets without producing glare off the wing, the wind-tunnel viewing glass, or the wind-tunnel floor that may have washed out targets or caused false targets.

AOA and wind speed were the independent variables during wind-tunnel testing. The yaw and roll angles were the control variables, held constant at 0 deg. The model was adjusted to the target AOA using the wind-tunnel controller. The actual AOA of the Nighthawk was confirmed using an inclinometer for each angle tested. The tested AOA were selected to correspond to lift coefficients (C_L) of slightly above 0.0 to slightly above 1.0 [25]. Here, the AOA was measured from the flat bottom of the Nighthawk to wind-tunnel horizontal as positioned on the sting. The geometry of the attachment of the wing to the fuselage creates the case in which a -5 deg AOA corresponds to a C_L of just greater than 0.0 and a 13 deg AOA corresponds to a C_L of just greater than 1.0 for all tested wind speeds.

In wind-tunnel testing it is common to set the wind speed and then perform a sweep of the AOA while holding the velocity constant. The camera positioning allowed for only a 10 deg variation in AOA before targets would be lost from view. As a result, the velocities were varied at each AOA rather than performing an AOA sweep for each velocity. The cameras were positioned to accommodate testing for a 3–13 deg AOA. Then the cameras were repositioned and tests were conducted for a -5–3 deg AOA.

At each of the 10 AOA at which the wings were tested, a static image set of the wing was captured before the wind tunnel was activated to establish the undeflected wing position. The velocity was then increased to 20 mph and held constant for about 30 s until transients died out. Image sequences were then captured and the process was repeated for the 30 and 40 mph cases. A second static (no-wind) image set was obtained after the 40 mph test was complete to compare with the first image set and ensure that the wing returned to its original location (i.e., the wing or model did not shift during the test).

Image sequences from the three synchronized cameras were captured at 75 fps for each of the 30 test cases listed in Table 1. A set of three simultaneous images, one from each camera, constitutes an image set, and the synchronized cameras produce one image set per frame. The three-dimensional location of each target on the wing was triangulated for each image set through the following videogrammetry process: target centers were marked to subpixel accuracy on all three images, the software then traced rays in space from each camera to the marked targets, and the three-dimensional global location of the targets was determined by the intersection of rays from multiple cameras. A local coordinate system was specified using coded targets 1, 2, and 3 in Fig. 4. Once the first frame in the captured image sequence has been processed (i.e., the three-dimensional location of each target has been solved), the targets can be tracked through the remaining frames. The location of each target in each frame can then be exported to a data file. The final result is a

Table 1 Test matrix

AOA, deg	Speed, mph	Ambient Pressure, torr	Temp, °F	*Re*
	21.1	731.8	71.9	91,317
−5.05	31.7	731.8	73.0	136,942
	42.1	732.3	73.3	181,857
	21.1	733.6	72.9	91,375
−2.9	31.8	733.6	73.6	137,529
	42.4	733.8	74.1	183,280
	21.4	733.8	73.3	92,656
−0.95	31.9	734.1	73.8	138,003
	42.4	734.1	73.9	183,410
	21.1	734.3	73.5	91,365
1.15	31.8	734.6	73.8	138,121
	42.6	734.3	74.1	184,297
	21.1	734.8	74.3	91,293
3.2	31.9	734.6	73.8	138,121
	42.7	734.6	74.2	184,763
	21.7	744.7	69.4	96,037
5.1	32.3	744.7	69.4	142,949
	43.1	744.5	68.8	190,924
	21.1	733.0	79.5	90,192
7.3	31.8	733.0	79.5	135,929
	42.1	733.0	79.5	179,957
	21.5	732.5	80.7	91634
9.4	32.2	732.3	81.2	137097
	42.1	732.3	82.0	178971
	21.4	731.3	81.4	90,951
11.4	31.6	731.3	81.4	134,302
	42.3	731.3	81.4	179,777
	21.4	731.3	81.8	90,881
13.4	31.5	731.3	81.8	133,773
	42.1	731.3	81.8	178,789

set of three-dimensional target locations in time. This process is summarized in Fig. 6.

The collinearity equations that trace rays from cameras to targets, relating the global three-dimensional target location (X, Y, Z) to the corresponding point (x, y) in the image plane, are [1,26]

$$x - x_p - dx = -c\frac{m_{11}(X - X_c) + m_{12}(Y - Y_c) + m_{13}(Z - Z_c)}{m_{31}(X - X_c) + m_{32}(Y - Y_c) + m_{33}(Z - Z_c)}$$

$$y - y_p - dy = -c\frac{m_{21}(X - X_c) + m_{22}(Y - Y_c) + m_{23}(Z - Z_c)}{m_{31}(X - X_c) + m_{32}(Y - Y_c) + m_{33}(Z - Z_c)} \tag{1}$$

where d_x and d_y are coordinate shifts caused by lens distortion.

In Eq. (1), the parameter set (c, x_p, y_p) is the interior orientation of the camera calculated during camera calibration, where c is the principal distance of the lens (focus), and x_p, and y_p are the principal-point coordinates on the image plane. ω, ϕ, κ, X_c, Y_c, and Z_c define the global three-dimensional orientation of a camera, where (ω, ϕ, κ) are the Euler rotational angles, and (X_c, Y_c, Z_c) are the coordinates of the perspective global center. The coefficients m_{ij} $(i, j = 1, 2, 3)$ are the rotation matrix elements that are functions of (ω, ϕ, κ) [1,26].

More detail on photogrammetry and videogrammetry processing and measurements can be found in [24,26–28].

III. Results

The videogrammetry processing yielded sets of three-dimensional point locations in time. The time history of one of these points is plotted in Fig. 7. This graph shows the out-of-plane z position of a single point on the wing during one of the wind-tunnel tests of the Nighthawk mini-UAV. The bottom graph of Fig. 7 shows the power spectral density (PSD) of that same point. In the frequency domain it is possible to see a peak at approximately 31 Hz.

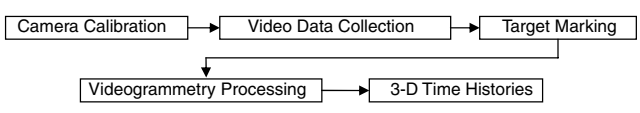

Fig. 6 Videogrammetry process.

Standard practice is to use videogrammetry to measure the static deflection shape of the wing over the course of test [5,8]. These data can be plotted in several ways, including the average deflected shape from the undeflected no-wind condition, examples of which are shown in Fig. 8; the standard deviation of the vibration from the average deflected shape, shown in Fig. 9; and the maximum deflection from the average deflected shape, discussed later. The average deflected shapes in Fig. 8 show that at low AOA most of the deflection occurs at the trailing-edge wing tip, causing twist, whereas at higher AOA the shapes involve more tip bending. The standard deviation from the average deflected shape in Fig. 9 shows that larger amplitude vibrations occur as expected at the most flexible part of the wing, the trailing-edge wing tip.

Figures 8 and 9 also demonstrate the limitation of videogrammetry measurements in wind-tunnel testing. Accurate measurements require deflection to be visible to the cameras, meaning any motion less than a pixel is unresolvable. The Nighthawk's wingspan is 66 cm, and the collected images were 1280×1024 pixels, yielding a camera resolution of approximately 0.5 mm/pixel. This resolution correlates to the maximum error of 0.62 mm measured in the calibration tests discussed earlier. The average deflected shapes shown in Fig. 8 on the order of several centimeters are well above the noise floor of the videogrammetry measurement and, correspondingly, appear smooth. The standard deviations of the vibration amplitude from the average deflected shapes in Fig. 9 are on the order of tens of microns, below the noise floor of the videogrammetry measurement. Correspondingly, these figures appear quite noisy, resulting in a lack of confidence in the results. Although the resolution limits of the cameras may minimize the usefulness of videogrammetry in standard rigid-wing wind-tunnel testing, their unique ability to capture large-amplitude motion well above the maximum threshold of laser measurement systems makes them well suited to these types of flexible-wing MAV measurements.

Power spectral densities of four points on the wing for the same case as in Fig. 7, the −0.95 deg AOA, 30 mph wind speed case, are shown in Fig. 10. Also shown are the targets on the wing corresponding to the plotted PSDs. Figure 10 confirms a peak frequency in the x and z directions around 31 Hz.

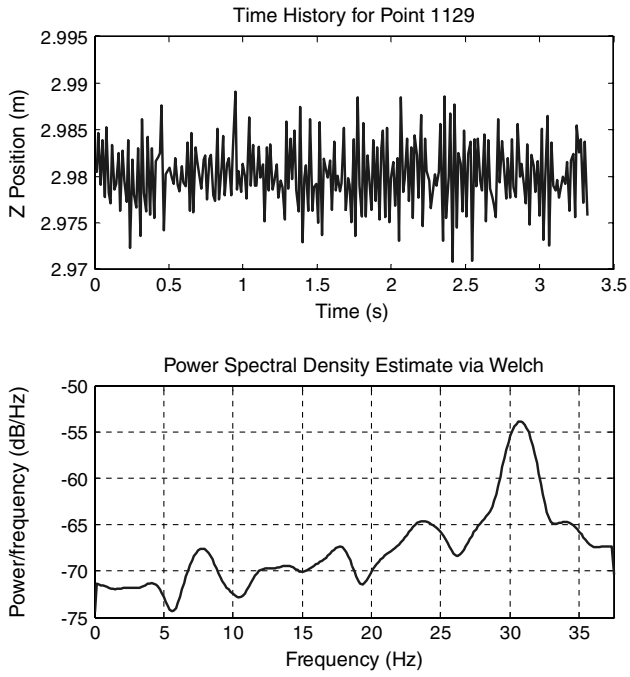

Fig. 7 Sample z direction: a) time history, and b) power spectral density.

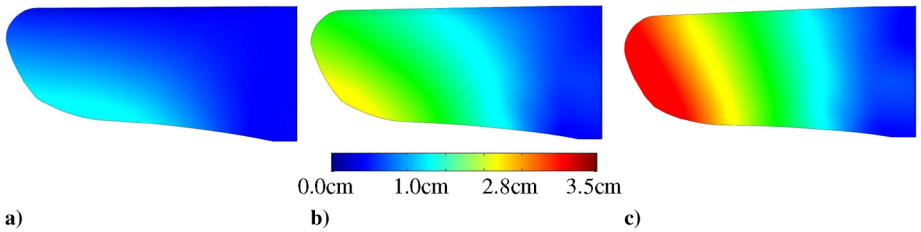

Fig. 8 Examples of average static deflected shapes of wing: a) −0.95 deg AOA, 30 mph wind speed; b) 5.1 deg AOA, 40 mph wind speed; c) 11.4 deg AOA, 40 mph wind speed.

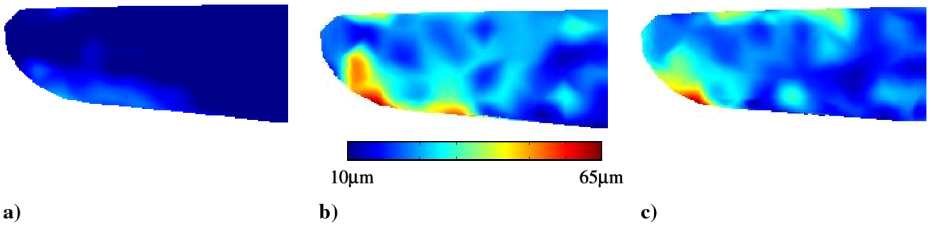

Fig. 9 Examples of standard deviation from average deflected shapes of wing: a) −0.95 deg AOA, 30 mph wind speed; b) 5.1 deg AOA, 40 mph wind speed; c) 11.4 deg AOA, 40 mph wind speed.

An examination of other AOA and wind speed cases in Figs. 11 and 12 demonstrates the capability of this videogrammetry method to characterize both large deflections on the order of centimeters and small deflections on the order of millimeters. Figure 11 shows a much higher peak, over −20 dB in one case, corresponding to much higher amplitude deflection in the wing than in the previous figures. Figure 12 shows a case in which, although some highly damped resonance is indicated in the *y* direction by the wide peak at 22.5 Hz, the motion is of such low amplitude that it is extremely difficult to visualize. In this case, it appears that either resonance motion does not occur, which would indicate that the wing does not experience flutter under these test conditions, resonance motion occurs at amplitudes below the resolution of the videogrammetry measurement, or resonance motion occurs at a frequencies above the measurement bandwidth of half the frame rate or 37.5 Hz. Note that higher frame rate cameras can be used to expand the dynamic range of measurement.

Further examination of Figs. 10–12 shows several instances in which peaks occur at the same frequencies in multiple directions. The best example is Fig. 11, in which there is clearly a peak in all three directions at 3.2 Hz. In the −0.95 deg AOA, 30 mph wind speed case in Fig. 10, peaks occur in the *x* and *z* directions at 29.5 Hz. Assuming that the peaks correspond to the first bending or first torsion mode of the wing, both in- and out-of-plane motion is expected in the *x* and *z* directions, whereas significantly less is expected in the *y* direction. *y*-direction-only resonance is expected for rigid-body rocking of the test article and fixture. Based on the directional coupling of peaks in the PSDs, suppositions can be made regarding the corresponding deflection shape, but another advantage of this videogrammetry technique is that it also enables shape visualization.

An important contribution of this technique is the capability to visualize the ODS corresponding to peaks in the frequency domain, as seen in the graphs in Figs. 10 and 11, by temporally filtering the time histories of the measured three-dimensional points, fitting a

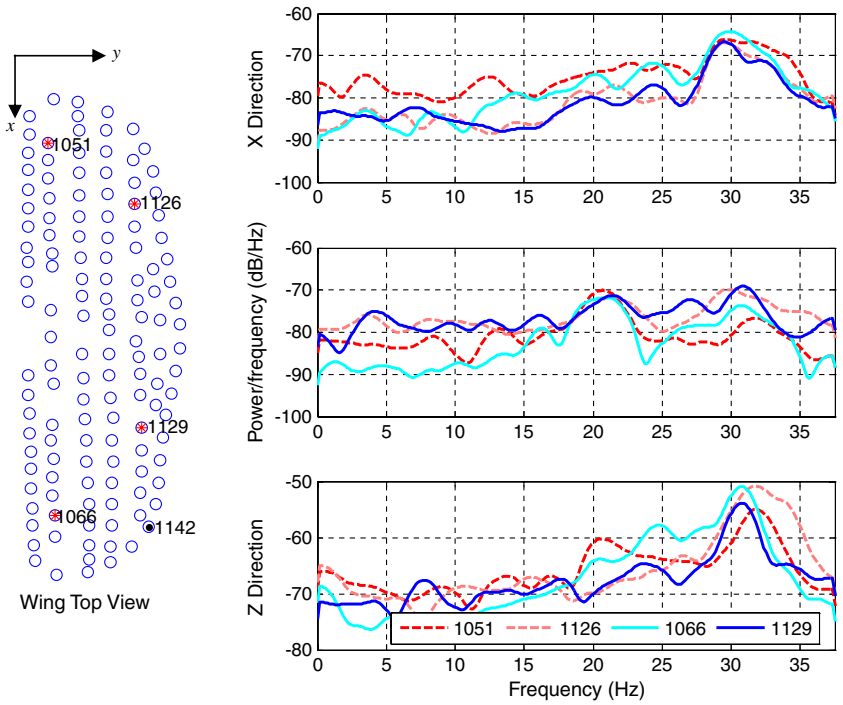

Fig. 10 Power spectral densities of multiple points for −0.95 deg AOA, 30 mph wind speed, *x*, *y*, and *z* directions.

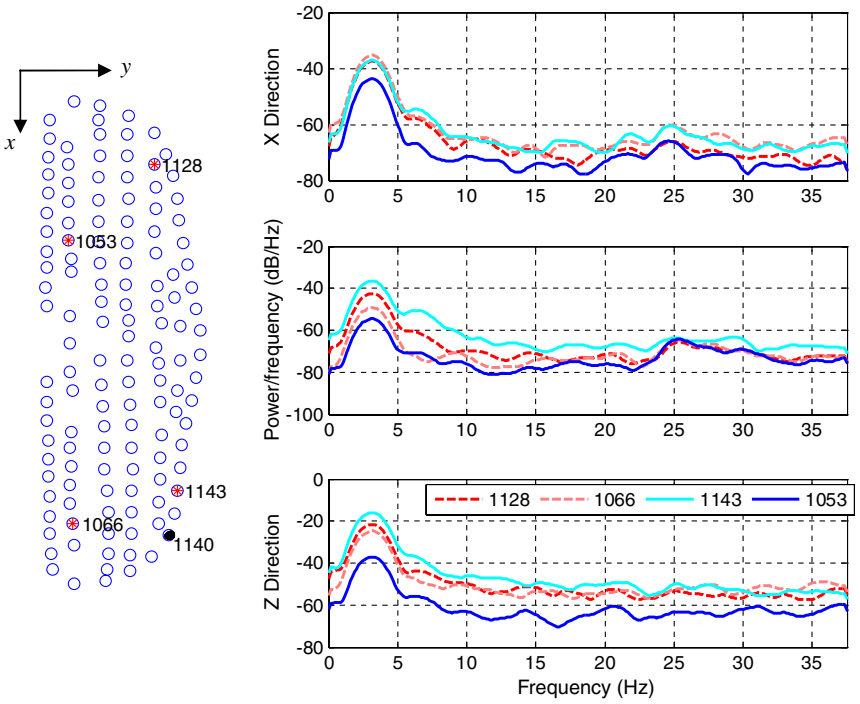

Fig. 11 Power spectral densities of multiple points for −0.95 deg AOA, 40 mph wind speed, *x*, *y*, and *z* directions.

surface to those points at each time step (frame), and animating the surface. Animating the ODS is a powerful tool that shows scaled asymmetric flapping behavior in Figs. 13a and 13b, corresponding to the peak at 3.2 Hz in the −0.95 deg AOA, 40 mph wind speed case. In addition to large-amplitude motion, the technique allows visualization of the small-amplitude in-plane rippling in the 3.2 deg AOA, 40 mph wind speed case, shown in Fig. 13c.

Summaries of the results of the visualization of the ODS corresponding to peaks in the PSDs of all test cases are listed in Table 2. Analysis shows that the flexible Nighthawk wing that was tested is susceptible to flapping at low and high angles of attack. A more complicated coupling between the first bending and first torsion modes of the wing is visible in the −0.95 deg AOA, 30 mph wind speed case. The asymmetric flapping, shown in Figs. 13a and 13b, appears to be very similar to the first structural mode shape observed in vibration testing of an earlier version of the wing using a laser vibrometer [20]. In those tests, however, the behavior occurred at 25 Hz, versus the 1–3 Hz observed in the low-AOA cases here. These results indicate that low-AOA flight conditions may experience vortex shedding or other aerodynamic excitations that are sufficient to induce high amplitude motion at frequencies much lower than structural resonances.

At the midrange AOA between 1.15 and 11.4 deg, the only apparent spectral content in the measured response of the wing is a highly damped rigid-body rocking mode that is likely a result of the fixing of the test article on a sting in the flow. The characterization of

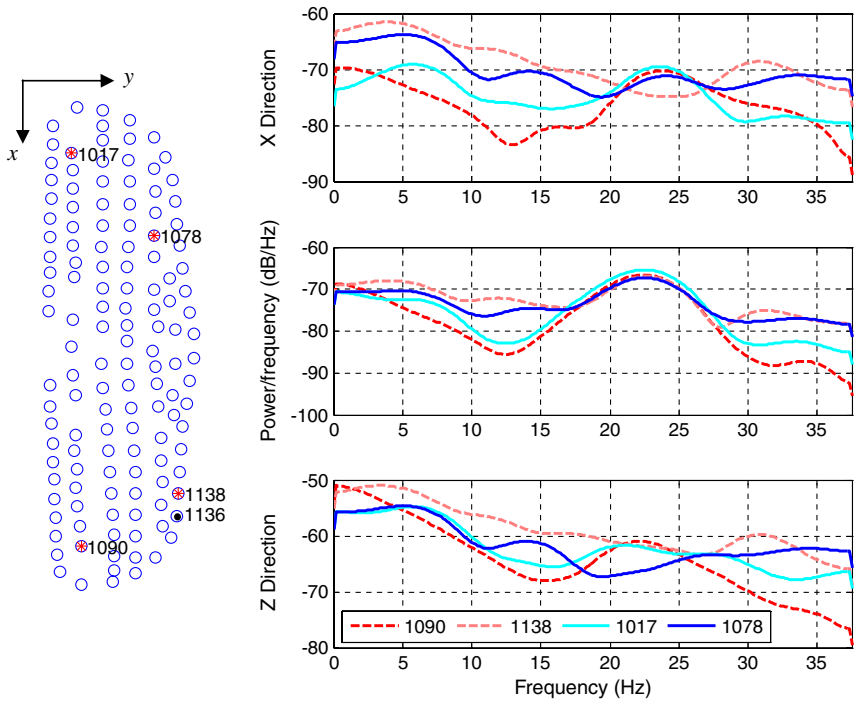

Fig. 12 Power spectral densities of multiple points for 13.4 deg AOA, 20 mph wind speed, *x*, *y*, and *z* directions.

Table 2 Test results

AOA, deg	Speed, mph	Resonance frequency, Hz	ODS comments	Max deflection z dir, cm
	21.1	Not visible	——	0.08
−5.05	31.7	1.3	Asymmetric flapping	1.50
	42.1	2.5	Asymmetric flapping	3.44
	21.1	21.3	Asymmetric flapping, noisy	0.03
−2.9	31.8	2.6	Asymmetric flapping	0.95
	42.4	2.6	Asymmetric flapping	2.53
	21.4	Not visible	——	0.04
−0.95	31.9	29.5	Coupled bending/torsion	0.11
	42.4	3.2	Asymmetric flapping	1.07
	21.1	Not visible	——	0.03
1.15	31.8	29.3	Possible rigid body rocking	0.04
	42.6	22.0	Possible rigid body rocking	0.10
	21.1	Not visible	——	0.04
3.2	31.9	29.6	Possible rigid body rocking	0.04
	42.7	21.5	Possible rigid body rocking	0.05
	21.7	Not visible	——	0.01
5.1	32.3	16.5, 28.9	Possible rigid body rocking	0.02
	43.1	21.5	Possible rigid body rocking	0.05
	21.1	22.0	Possible rigid body rocking	0.02
7.3	31.8	Not visible	——	0.03
	42.1	21.5	Possible rigid body rocking	0.05
	21.5	21.7, 27.8	Possible rigid body rocking	0.03
9.4	32.2	21.7, 29.5	Rigid body rocking at 21.7	0.02
	42.1	21.7	Possible rigid body rocking	0.04
	21.4	22.3	Rigid body rocking, noisy	0.02
11.4	31.6	29.6	Rigid body rocking, noisy	0.04
	42.3	22.0	Possible rigid body rocking	0.05
	21.4	22.5	Rocking / flapping	0.06
13.4	31.5	22.0	Rocking / flapping	0.08
	42.1	24.6	Rocking / flapping	0.15

ODSs as presented here is a critical component in the validation of numerical models and simulations and the design, optimization, and control of lightweight flexible aerospace structures.

Table 2 also shows the measured maximum wing deflection from the average deflected shape (Fig. 8) for each of the test cases. These results are plotted in Fig. 14. This graph clearly demonstrates that, at 20 mph, the wings experience very low vibration amplitudes at any of the measured AOA, indicating that there should be little chance of induced instabilities. This conclusion is supported by the data in Table 2, which show only a couple of cases in which any spectral content was visible at 20 mph. Also confirming results from Table 2, Fig. 14 shows that, at low AOA, substantial motion was recorded for the 30 and 40 mph wind speed cases. A slight increase in deflection is also visible at the 13.4 deg AOA. Figures 10–12 show the location on the wing at which the maximum deflection from the average deflected shape occurred, indicated by the solid markers. As expected, in all cases the maximum deflection occurred at the trailing edge of the wing, away from both the rigid leading edge and aircraft body.

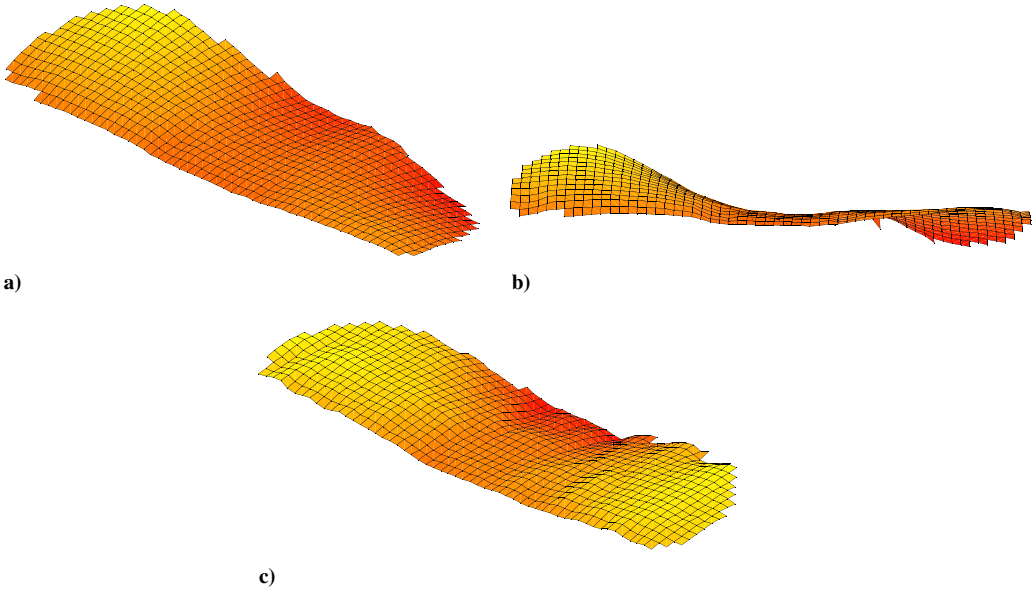

Fig. 13 Frames of animated deflection shapes of wing: a) three-dimensional pictorial view of −0.95 deg AOA, 40 mph wind speed at 3.2 Hz; b) front view of −0.95 deg AOA, 40 mph wind speed at 3.2 Hz; c) three-dimensional pictorial view of 3.2 deg AOA, 40 mph wind speed with no filter.

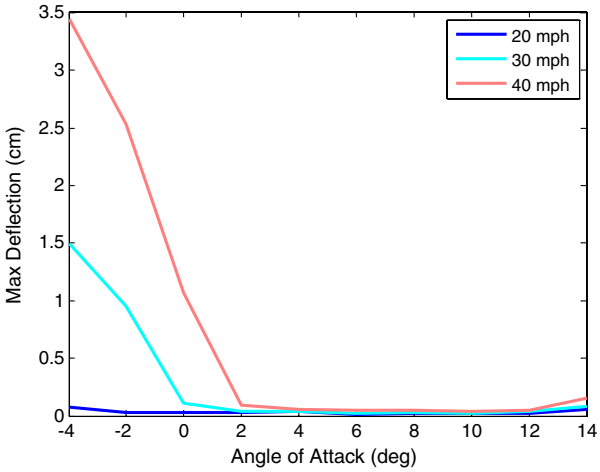

Fig. 14 Plots of maximum recorded deflection vs angle of attack.

These results indicate that the Nighthawk wing should be stable in most flight regimes with the exception of high-speed, low-AOA cases.

The maximum wing deflection from average deflected shape values reported in Table 2 helps to clarify the accuracy of the videogrammetry measurements. In most cases in which the ODS is inconclusive, there is a small maximum deflection, less than 0.5 mm. The clearest ODSs occurred in test cases in which the maximum deflection of the wing was greater than 0.5 mm. This conclusion coincides with the camera pixel resolution threshold discussed earlier, resulting in high confidence in the resonance frequencies and corresponding ODS extracted through this extension of videogrammetry.

Unconventional data such as wing damping may also be extracted spectrally from the videogrammetry data through the half-power or other method [29], and the technique can also measure in-plane strain and curvature with smaller targets [30].

IV. Conclusions

The presented work uses noncontact videogrammetry measurement techniques to analyze flexible, lightweight carbon fiber composite mini-UAV wings in wind-tunnel testing. These flexible wings are of interest due to their stability in flight and low mass. The wind-tunnel data here show the wing to be very stable at all tested wind speeds, up to 40 mph, for AOA greater than 0 deg. The wing only exhibited flapping behavior at negative AOA, corresponding to low C_L, and at much lower frequencies than structural resonance. The flexible nature of the wing was evident in the large deflections of over 3.4 cm it experienced in these cases.

The videogrammetry technique used here extends previous measurements to capture the resonance frequencies and corresponding operating deflection shapes of the wings over the measured range of AOA and wind speeds. This technique allowed the observed flapping behavior to be distinguished from the rigid body rocking of the test fixture. The knowledge of the deflection shape of the wing at different resonance frequencies is necessary to understand the complicated membrane-structure interactions as MAVs become smaller and lighter and to validate structural, aeroelastic, and aerodynamic numerical models; optimize wing aerodynamic performance as a function of angle of attack, Reynolds number, and geometry; and control flutter. The presented data show that videogrammetry will play a key role in the development of future lightweight MAV systems.

Acknowledgments

The authors would like to thank Jay Anderson, John Hixenbaugh, Chris Zickefoose, and Tina Reynolds of the U.S. Air Force Institute of Technology Department of Aeronautics and Astronautics for their assistance with model preparation and wind tunnel operation. We would also like to thank the Control Analysis and Design Branch of the U.S. Air Force Research Laboratory for sponsoring the research and Applied Research Associates, Inc., for supplying the test article and CAD geometry.

References

[1] Burner, A. W., and Liu, T., "Videogrammetric Model Deformation Measurement Technique," *Journal of Aircraft*, Vol. 38, No. 4, 2001, pp. 745–754. doi:10.2514/2.2826

[2] Barrows, D. A., "Videogrammetric Model Deformation Measurement Technique for Wind Tunnel Applications," AIAA Paper 2007-1163, Jan. 2007.

[3] Simpson, A., Rowe, J., Smith, S., and Jacob, J., "Aeroelastic Deformation and Buckling of Inflatable Wings Under Dynamic Loads," AIAA Paper 2007-2239, April 2007.

[4] Graves, S. S., Burner, A. W., Edwards, J. W., and Schuster, D. M., "Dynamic Deformation Measurements of an Aeroelastic Semispan Model," *Journal of Aircraft*, Vol. 40, No. 5, 2003, pp. 977–984. doi:10.2514/2.6883

[5] Albertani, R., Stanford, B., Hubner, J. P., and Ifju, P. G., "Aerodynamic Coefficients and Deformation Measurements on Flexible Micro Air Vehicle Wings," *Journal of Experimental Mechanics*, Vol. 47, No. 5, 2007, pp. 625–635. doi:10.1007/s11340-006-9025-5

[6] Stanford, B., Ifju, P., Albertani, R., and Shyy, W., "Fixed Membrane Wings for Micro Air Vehicles: Experimental Characterization, Numerical Modeling, and Tailoring," *Progress in Aerospace Sciences*, Vol. 44, No. 4, 2008, pp. 258–294. doi:10.1016/j.paerosci.2008.03.001

[7] Meyn, L., and Bennett, M. S., "A Two Camera Video Imaging System with Application to Parafoil Angle of Attack Measurements," AIAA Paper 91-0673, Jan. 1991.

[8] Fleming, G. A., Bartram, S. M., Waszak, M. R., and Jenkins, L. N., "Projection Moiré Interferometry Measurements of Micro Air Vehicle Wings," Society of Photo-Optical Instrumentation Engineers Paper 4448-16, July 2001.

[9] Black, J. T., Smith, S. W., Leifer, J., and Bradford, L., "Measuring and Modeling the Dynamics of Stiffened Thin Film Polyimide Panels," *Journal of Guidance, Control, and Dynamics*, Vol. 31, No. 3, 2008, pp. 490–500. doi:10.2514/1.32236

[10] Pappa, R. S., Black, J. T., Blandino, J. R., Jones, T. W., Danehy, P. M., and Dorrington, A. A., "Dot Projection Photogrammetry and Videogrammetry of Gossamer Space Structures," *Journal of Spacecraft and Rockets*, Vol. 40, No. 6, 2003, pp. 858–867. doi:10.2514/2.7047

[11] Flint, E., Bales, G., Glaese, R., and Bradford, R., "Experimentally Characterizing the Dynamics of 0.5 m Diameter Doubly Curved Shells Made from Thin Films," AIAA Paper 2003-1831, April 2003.

[12] Riskin, D. K., Willis, D. J., Iriarte-Diaz, J., Hedrick, T. L., Kostandov, M., Chen, J., Laidlaw, D. H., Breuer, K. S., and Swartz, S. M., "Quantifying the Complexity of Bat Wing Kinematics," *Journal of Theoretical Biology*, Vol. 254, 2008, pp. 604–615. doi:10.1016/j.jtbi.2008.06.011

[13] Iriarte-Diaz, J., and Swartz, S. M., "Kinematics of Slow Turn Maneuvering in the Fruit Bat Cynopterus Brachyotis," *Journal of Experimental Biology*, Vol. 211, 2008, pp. 3478–3489. doi:10.1242/jeb.017590

[14] Willis, M. A., and Avondet, J. L., "Odor-Modulated Orientation in Walking Male Cockroaches *Periplaneta Americana*, and the Effects of Odor Plumes of Different Structure," *Journal of Experimental Biology*, Vol. 208, 2005, pp. 721–735. doi:10.1242/jeb.01418

[15] Sane, S. P., Dieudonné, A., Willis, M. A., and Daniel, T. L., "Antennal Mechanosensors Mediate Flight Control in Moths," *Science*, Vol. 315, Feb. 2007, pp. 863–866. doi:10.1126/science.1133598

[16] Liu, T., Kuykendoll, K., Rhew, R., and Jones, S., "Avian Wing Geometry and Kinematics," *AIAA Journal*, Vol. 44, No. 5, 2006, pp. 954–963. doi:10.2514/1.16224

[17] Curtis, D. H., Reeder, M. F., Svanberg, C. E., and Cobb, R. G., "Flapping Wing Micro Air Vehicle Bench Test Setup," AIAA Paper 2009-1272, Jan. 2009.

[18] Pitcher, N. A., and Maple, R. C., "A Static Aeroelastic Analysis of a Flexible Wing Mini Unmanned Aerial Vehicle," AIAA Paper 2008-

4057, June 2008.
[19] Pitcher, N. A., "A Static Aeroelastic Analysis of a Flexible Wing Mini Unmanned Aerial Vehicle," Master's Thesis, Department of Aeronautics and Astronautics, U.S. Air Force Institute of Technology, March 2008.
[20] Stults, J., Maple, R., Cobb, R., and Parker, G., "Computational Aeroelastic Analysis of Micro Air Vehicle with Experimentally Determined Modes," AIAA Paper 2005-4614, June 2005.
[21] Ifju, P., Jenkins, D. A., Ettinger, S., Lian, Y., Shyy, W., and Waszak, M. R., "Flexible-Wing-Based Micro Air Vehicles," AIAA Paper 2002-0705, Jan. 2002.
[22] Shyy, W., Klevebring, F., Nilsson, M., Sloan, J., Carroll, B., and Fuentes, C., "Rigid and Flexible Low Reynolds Number Airfoils," *Journal of Aircraft*, Vol. 36, No. 3, 1999, pp. 523–529. doi:10.2514/2.2487
[23] DeLuca, A. M., Reeder, M. F., Freeman, J., and Ol, M. V., "Flexible- and Rigid-Wing Micro Air Vehicle: Lift and Drag Comparison," *Journal of Aircraft*, Vol. 43, No. 2, 2006, pp. 572–575. doi:10.2514/1.15643
[24] *PhotoModeler 6 User Guide*, 1st ed., Eos Systems, Inc., Jan. 2007.
[25] Anderson, J. D., *Introduction to Flight*, 6th ed., McGraw–Hill, New York, 2006, ISBN 0071263187.
[26] Wong, K. W., "Basic Mathematics of Photogrammetry," *Manual of Photogrammetry*, 4th ed., edited by C. C. Slama, American Society of Photogrammetry, Falls Church, VA, 1980, Chap. 2, pp. 37–101.
[27] Mikhail, E. M., Bethel, J. S., and McGlone, J. C., *Introduction to Modern Photogrammetry*, Wiley, New York, 2001, ISBN 0471309249.
[28] Atkinson, K. B., *Close Range Photogrammetry and Machine Vision*, Whittles Publishing, Caithness, Scotland, 2001, ISBN 1870325737.
[29] Inman, D. J., *Vibration with Control, Measurement, and Stability*, Prentice–Hall, Upper Saddle River, NJ, 1989, ISBN 0139427988.
[30] Leifer, J., Black, J. T., Smith, S. W., Ma, N., and Lumpp, J. K., "Measurement of In-Plane Motion of Thin-Film Structures Using Videogrammetry," *Journal of Spacecraft and Rockets*, Vol. 44, No. 6, Nov.–Dec. 2007, pp. 1317–1325. doi:10.2514/1.25566; also AIAA Paper 2006-1805, 2006.